Journal of Physics: Conference Series **2934** (2025) 012012 doi:10.1088/1742-6596/2934/1/012012

Multi-wavelength Analysis of the Vela X Pulsar Wind Nebula: Leptonic Emission from Fermi-LAT, Suzaku, and H.E.S.S.

Supphakit Wiweko[1,2], Brandon Khan Cantlay[1,2], Maneenate Wechakama[1,2*] and Siraprapa Sanpa-arsa[2]

[1]Department of Physics, Faculty of Science, Kasetsart University, Bangkok, 10900, Thailand
[2]National Astronomical Research Institute of Thailand (Public Organization), Chiangmai, 50180, Thailand

E-mail: maneenate.w@ku.th

Abstract. Pulsar wind nebulae (PWNe) are a significant source of very-high-energy gamma rays in the Milky Way. These fascinating objects arise from the interaction between the powerful winds emanating from a central, rapidly rotating pulsar and the expanding debris field left behind by a supernova remnant. This study aims to explain the high-energy emissions from three significant compact regions around the Vela pulsar wind nebula through leptonic spectral energy distribution (SED) emissions across multiple wavelengths. We analyze the SED of photons using 15 years of Fermi-LAT data in the 100 MeV to 1 TeV range and combine these data with other observations, such as those from Suzaku (X-ray) and H.E.S.S. (very-high-energy gamma-ray). We then model leptonic SED emissions to produce non-thermal radiation, including synchrotron radiation and inverse Compton scattering, to find the best fit with the observed multi-wavelength spectra. By analyzing the multi-wavelength emission from the Vela pulsar wind nebula, we constrain the properties of relativistic particles, magnetic fields, and interstellar radiation fields that contribute to this observed radiation.

1 Introduction

1.1 Pulsars and Pulsar wind nebulae

Pulsar wind nebulae (PWNe) are captivating cosmic creations. These vast nebulae, sculpted by the energetic winds of rapidly spinning pulsars interacting with their surroundings, radiate across the electromagnetic spectrum [12] [14][19]. The diversity in their light distribution and overall shapes hints at the complex interplay between particle motion and various cooling mechanisms within them.

A prime example lies within the Vela supernova remnant (SNR), a mere 290 pc away. This SNR harbors a captivating resident, the young pulsar PSR B0833-45 [10]. This 11,000-year-old object, boasts a characteristic age and spins down at an impressive rate, releasing a luminosity of 7×10^{36} erg s^{-1} [17]. The SNR itself is renowned for its non-thermal emission regions, like the radio-bright Vela X. PSR B0833-45, a close-by adolescent pulsar with a rapid 89-millisecond rotation period [16], has been extensively studied across the spectrum, from radio and gamma-ray [20] to optical and X-ray wavelengths, including additional gamma-ray bands [13]. Interestingly, this powerhouse releases a tremendous amount of spin-down energy, with its peak electromagnetic emission concentrated in the GeV gamma-ray band. Understanding the light emitted by such objects is crucial. Two key mechanisms are at play: synchrotron radiation and inverse Compton scattering. By analyzing the combined X-ray and gamma-ray emissions alongside models that incorporate these processes, astronomers can glean valuable insights into the behavior of particles within PWNe (e.g., [9][7][4]). This allows for the validation of complex simulations and furthers our understanding of these remarkable objects.

Journal of Physics: Conference Series **2934** (2025) 012012 doi:10.1088/1742-6596/2934/1/012012

2 Observations and Regions of Interest

2.1 Gamma-Ray Data from Fermi-LAT

The Large Area Telescope (LAT) onboard the Fermi Gamma-ray Space Telescope (FGST) revolutionized gamma-ray astronomy [8]. It detects gamma rays via pair-conversion into electron-positron pairs within its high-resolution converter tracker, enabling precise directional measurements [8]. The LAT also features a CsI(Tl) crystal calorimeter for energy determination and an anti-coincidence detector for efficient background rejection [1]. Compared to previous instruments, LAT boasts significant improvements: a larger effective area (reaching $\sim$ 8000 cm^2 on-axis above 1 GeV), a wider field of view (FOV; $\sim$2.4 sr), and superior angular resolution ($\sim 0.6^\circ$ for 68% containment at 1 GeV for events converting in the front section of the tracker) [8]. For a detailed description of the instrument and data processing techniques [2].

For this specific analysis, we leveraged 15 years of data collected by the Fermi-LAT, spanning from August 4, 2008 to March 28, 2024. To ensure the highest-quality data, we exclusively included gamma rays classified as "Diffuse class events" (indicating the most stringent background rejection). Additionally, we excluded events with a zenith angle larger than 90° relative to the detector axis to minimize potential contamination by Earth-albedo photons. The instrument response functions (IRFs) employed in this analysis are the `P8R3 V3`, that incorporate corrections for pile-up and accidental coincidence effects arising within the detector subsystems. Furthermore, we utilized the `gll iem v07` model for the galactic diffuse emission and the `iso P8R3 SOURCE V3 v1` model for the isotropic diffuse emission. Our source identification is based on the latest Fermi-LAT 12-year Source Catalog (4FGL-DR3), which incorporates 12 years of survey data across the 50 MeV – 1 TeV energy range [3].

2.2 Regions of Interest

We define three spectral extraction regions (pointing regions 0, 1, and 2) for Fermi-LAT data analysis (Figure 1), corresponding to the pointing positions used by Suzaku and H.E.S.S. observations. These square regions, each with a side length of 7.50", are centered at 128.81°, Dec = −45.286° (pointing 0), RA = 128.7666°, Dec = −45.4581°(pointing 1), and RA = 128.6368°, Dec = −45.8007° [1]. This approach facilitates a multi-wavelength SED analysis using data from Fermi-LAT, Suzaku, and H.E.S.S.

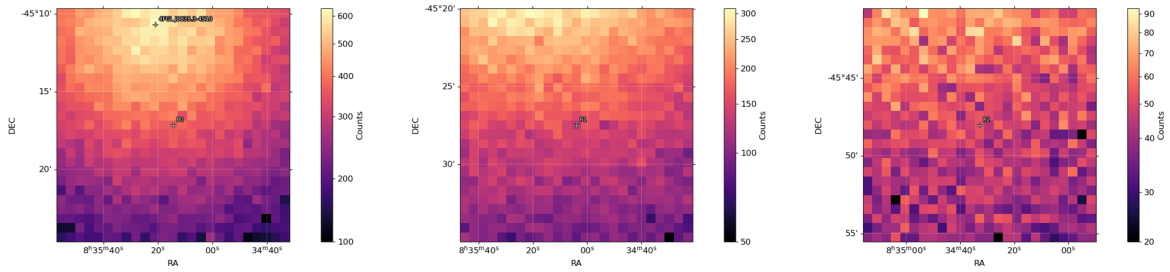

Figure 1: Spectral analysis regions for the Vela X pulsar wind nebula in Fermi-LAT data. The top, middle, and bottom panels correspond to pointing regions 0, 1, and 2, respectively [1].

3 Spectral Analysis

The Fermi-LAT spectrum was constructed by binning the 100 MeV to 1 TeV energy range into seven logarithmically spaced energy intervals. A maximum likelihood analysis was then performed on each bin to derive the spectrum [21], assuming a power-law shape for the spectral energy distribution (SED) of the Vela X source.

$$\frac{dN_\gamma}{dE} = A(\frac{E}{E_0})^{-\alpha} \tag{1}$$

where $\frac{dN_\gamma}{dE}$ is the photon flux from Fermi-LAT , E_0 is the referent energy which we set $E_0 = 1000$ MeV, A is amplitude, α is the power law index.

We employed a consistent spatial model for all three regions: a radial disk with a characteristic width of 0.125° (details in Table 1), as described in Section 2.2. This model represents the extended gamma-ray emission observed by the Fermi-LAT. Assuming this spatial morphology, the Fermi-LAT detects the

gamma-ray source with a high significance of 14 in the broad 100 MeV to 1 TeV energy range. The resulting spectrum, normalized to the entire phase interval for consistency, is presented in Figure 2.

We employed a maximum likelihood analysis to fit a power-law spectral model to the data within the 100 MeV to 1 TeV energy range. The Test Statistic (TS) values for each region are presented in Table 1. This approach, offering greater reliability than a direct fit to the individual spectral points in Figure 2, demonstrates that the data (Table 1) is well-characterized by a power law for pointing regions 0, 1, and 2, with respective spectral indices of -2.74 ± 0.259, -2.77 ± 0.11, and -2.48 ± 0.00291, respectively.

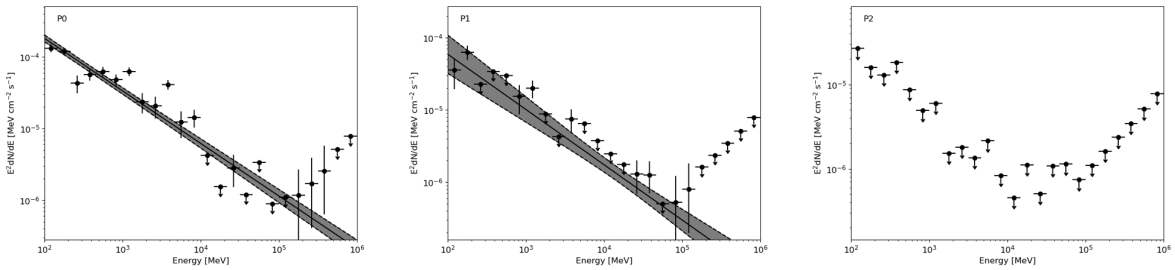

Figure 2: Spectral Energy Distribution (SED) for three distinct regions within the Vela complex. The Fermi-LAT data points represent the binned photon flux in seven logarithmic energy bins from 100 MeV to 1 TeV, obtained using a maximum likelihood analysis. Error bars indicate the associated uncertainties.

Table 1: Best-fit parameters for the photon SED of the Vela PWN of Fermi-LAT observation in the three regions

Pointing	Spatial model	Spectrum type	α	TS
0	Radial Disk	Power law	-2.74 ± 0.259	218.75
1	Radial Disk	Power law	-2.77 ± 0.11	40.41
2	Radial Disk	Power law	-2.48 ± 0.00291	0.08

4 Synchrotron Radiation and Inverse Compton Scattering as an Explanation of Photon Spectrum of Vela X PWN

We will use non-thermal radiation mechanisms, i.e., synchrotron and inverse Compton (IC) emission, to explain multi-wavelength observations of Vela X from the Suzaku spectrum in X-ray, the H.E.S.S. spectrum in gamma-ray, and the Fermi-LAT gamma-ray spectrum analyzed in this work. We assume a leptonic energy distribution with an exponential cutoff:

$$\frac{dN_e}{dE} = A(\frac{E_e}{E_0})^{-\alpha} exp(-\frac{E_e}{E_c})^{\beta}, \tag{2}$$

where N_e is the electron density number, E_e is the lepton energy, A is amplitude, α is the power law index, E_0 is reference energy this work $E_0 = 1\ TeV$, E_c is the cutoff energy, and β is the cutoff exponent.

We use the **naima** Python package to calculate SED models and find the best-fit with observed multiwavelength data. [22]. This package leverages established formalisms to compute the different emission components: synchrotron radiation is calculated based on the method described in [6], while IC emission utilizes the formalisms presented in [15] and [5]. For the synchrotron emission:

$$Q_{Syn} = \int_0^{\infty} n_e P_{syn}(\nu, \gamma, B) d\gamma, \tag{3}$$

with $P_{syn}(\nu, \gamma, B)$ represents the power emitted by a single relativistic electron via synchrotron radiation. This expression can be written as

$$P_{syn}(\nu, \gamma, B) = \frac{\sqrt{3}}{2\pi} \frac{e^3 B}{m_e c^2 E_\gamma} F(\frac{E_\gamma}{E_c}), \tag{4}$$

and

$$F(x) = x\int_0^\infty K_{5/3}(\tau)d\tau, E_c = \frac{3eB\gamma^2}{2m_e c}, \tag{5}$$

where E_c is the critical frequency, $K_{5/3}$ denotes the modified Bessel function of order 5/3. For the emission of IC scattering:

$$Q_{ics} = \int_0^\infty n_e P_{ics}(\nu,\gamma)d\gamma, \tag{6}$$

with $P_{ics}(\nu,\gamma)$ represents the differential scattered photon spectrum per electron, which can be expressed as

$$P_{ics}(\nu,\gamma) = \frac{\sqrt{3}}{4}\frac{\sigma_T c}{\gamma^2}\int_0^\infty \frac{n_\gamma}{\nu_i} f(q,\Gamma_\epsilon)d\nu_i, \tag{7}$$

Here, ν_i denotes the frequency of the scattered photon. The target photon fields contributing to the scattering include the cosmic microwave background (CMB), galactic far-infrared (FIR) background, and near-infrared (NIR) and optical fields from stars and synchrotron emission. The function $f(q,\Gamma_\epsilon)$, incorporating the Klein-Nishina cross-section, is expressed as

expressed as

$$f(q,\Gamma_\epsilon) = 2qlnq + (1+q)((1+2q) + \frac{1}{2}\frac{(\Gamma_\epsilon q)^2}{(1+\Gamma_\epsilon q)}, \tag{8}$$

with

$$q = \frac{h\nu}{\Gamma_\epsilon(\gamma m_e c^2 - h\nu)} and \Gamma_\epsilon = 4\gamma h\nu_i/m_e c^2. \tag{9}$$

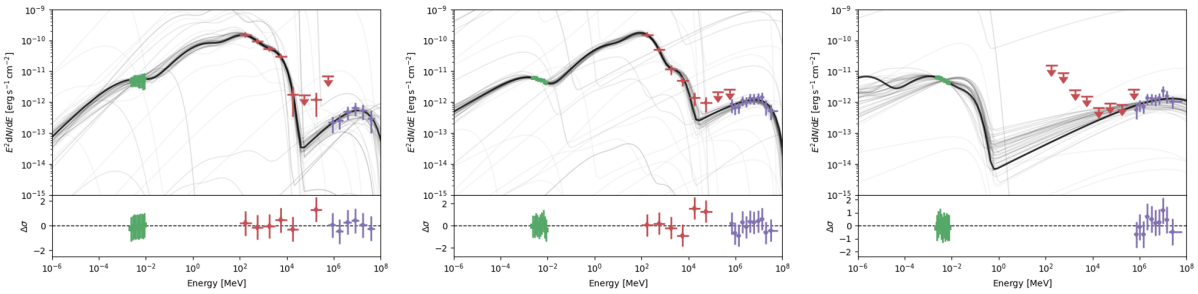

Figure 3: Multi-wavelength best-fit spectral energy distributions (SEDs) for the three pointing regions. Suzaku XIS X-ray measurements are shown in green. H.E.S.S. gamma-ray measurements are shown in purple [1]. Fermi-LAT gamma-ray measurements (this work) are shown in red, with the upper limit indicated by the red line.

Table 2: Best-fit parameters for the leptonic energy distribution of the Vela PWN of the three regions using multi-wavelength SEDs

Pointing	Population of lepton	$W_e(>1TeV)(10^{44}erg)$	α	E_c (MeV)	β	B(μG)
0	1	0	$1.4^{+0.2}_{-0.2}$	$2.3^{+0.6}_{-0.6}\times10^4$	$2.0^{+0.3}_{-0.2}$	$7.0^{+1.1}_{-1.0}$
	2	0.421	$1.5^{+0.3}_{-0.1}$	$9.2^{+14}_{-5}\times10^7$	$1.4^{+0.3}_{-0.3}$	$7.0^{+1.1}_{-1.0}$
1	1	0	$1.7^{+0.2}_{-0.2}$	$3.1^{+1.6}_{-1.0}\times10^4$	$2.9^{+0.3}_{-0.2}$	$7.2^{+0.6}_{-0.7}$
	2	1.246	$2.1^{+0.2}_{-0.2}$	$9.6^{+24.3}_{-3.3}\times10^7$	$3.1^{+0.3}_{-0.2}$	$7.2^{+0.6}_{-0.7}$
2	1	2.150	$2.3^{+0.2}_{-0.2}$	$3.4^{+0.8}_{-0.8}$	$0.05^{+0.01}_{-0.01}$	$3.8^{+0.7}_{-1.0}$
	2	0	$1.3^{+0.3}_{-0.3}$	$8.1^{+3.4}_{-2.1}$	$1.0^{+0.1}_{-0.1}$	$3.8^{+0.7}_{-1.0}$

Table 3: Properties of the target photon fields

Pointing	NIR temperature (K)	NIR energy density (eV cm^{-3})	FIR temperature (K)	FIR energy density (eV cm^{-3})
0	2954^{+3081}_{-681}	$0.29^{+0.07}_{-0.07}$	124^{+46}_{-33}	$0.62^{+0.1}_{-0.1}$
1	2707^{+1109}_{-739}	$0.1^{+0.02}_{-0.02}$	96^{+34}_{-27}	$1.2^{+0.02}_{-0.03}$
2	2728^{+814}_{-595}	$1.0^{+0.01}_{-0.01}$	63^{+64}_{-41}	$0.3^{+0.2}_{-0.1}$

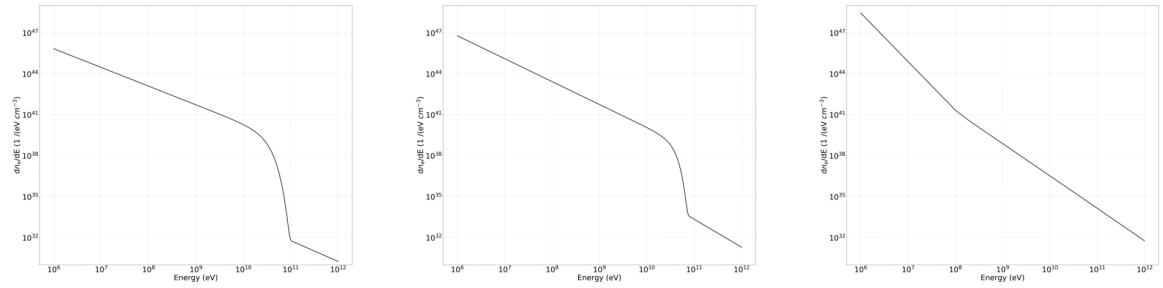

Figure 4: Combined leptonic energy distributions

To find the most compatible model parameters for our SED data, we utilized the naima package [22] alongside the Markov Chain Monte Carlo (MCMC) implemented in emcee [11]. While naima estimates these parameters and their probability distributions based on a chi-square analysis assuming Gaussian and uncorrelated uncertainties.

Our results are presented in Figure 3 and Table 2. Figure 3 compares the best-fit leptonic model (including model uncertainties) to the measured SEDs. This figure demonstrates that the leptonic models can reproduce the observed X-ray and gamma-ray SEDs for reasonable model parameters. Table 2 lists the best-fit parameters for two leptonic populations, following the approach of [18]. These parameters are presented alongside the median values and upper/lower uncertainties for the magnetic field within the Vela PWN. The properties of the target photons used for inverse Compton (IC) calculations are provided in Table 3.

We also present the combined leptonic energy distributions and additional leptonic energy distributions in Figure 4, which produced the best-fitting parameters detailed in Table 2 for the energy range from 1 MeV to 1 TeV.

The analysis reveals that synchrotron radiation and inverse Compton (IC) scattering models provide a good fit for pointing regions 0 and 1, effectively matching the observed data from Suzaku XIS in X-ray wavelengths and H.E.S.S. in gamma-ray wavelengths. Despite this, deviations are observed in some data points from the Fermi-LAT observations, indicating discrepancies with the model predictions. Conversely, in pointing region 2, the synchrotron and IC scattering models demonstrate robust performance, accurately describing the observed spectra across multiple wavelengths. However, the Fermi-LAT data for this region does not align well with the model predictions, suggesting potential limitations in the current model framework.

5 Summary

This study presents a comprehensive analysis of the Vela X pulsar wind nebula (PWN) using multi-wavelength data from the Fermi-LAT (gamma-ray), Suzaku (X-ray), and H.E.S.S. (gamma-ray) instruments. We divided the nebula into three distinct regions to enable a detailed spectral investigation. A power-law distribution was consistently found across the gamma-ray spectra for all three regions, suggesting a common particle acceleration mechanism responsible for the observed non-thermal emission.

To interpret the multi-wavelength data spanning X-ray and gamma-ray bands, we employed a sophisticated leptonic model. This model posits that high-energy electrons within the nebula emit radiation through synchrotron processes in the X-ray band and inverse Compton scattering in the gamma-ray band. Our findings suggest that a two-population distribution of these high-energy electrons provides the best fit for the observational data. This approach allowed us to derive the parameters of the nebula,

including the strength of its magnetic field, the characteristics of the ambient photon distribution, and the properties of the electron populations themselves.

The derived best-fit parameters offer valuable insights into the physical conditions and processes occurring within the Vela X nebula. Specifically, they shed light on the energy distribution of the electrons and the interaction between these particles and the nebular environment.

Looking forward, future research will aim to refine this leptonic model further. This will involve incorporating systematic uncertainties to improve the robustness of our conclusions. In addition, we plan to utilize data from upcoming observational missions, which will provide higher resolution and more comprehensive coverage of the nebula. These efforts will enhance our understanding of the complex dynamics and emission mechanisms at play in the Vela X pulsar wind nebula, contributing to the broader field of high-energy astrophysics.

6 ACKNOWLEDGEMENT

We would like to express our deepest appreciation to Dr. Armelle Jardin-blicq for her help and suggestions to analyze spectra from Fermi-LAT data. We also acknowledge the use of the CHALAWAN-NARIT high-performance computing cluster.

References

[1] H. Abdalla, F. Aharonian, F. A. Benkhali, E. O. Angüner, M. Arakawa, C. Arcaro, C. Armand, M. Backes, M. Barnard, Y. Becherini, et al. Hess and suzaku observations of the vela x pulsar wind nebula. *Astronomy & Astrophysics*, 627:A100, 2019.

[2] A. A. Abdo, M. Ackermann, W. Atwood, R. Bagagli, L. Baldini, J. Ballet, D. Band, G. Barbiellini, M. G. Baring, J. Bartelt, et al. Fermi large area telescope observations of the vela pulsar. *The Astrophysical Journal*, 696(2):1084, 2009.

[3] S. Abdollahi, F. Acero, L. Baldini, J. Ballet, D. Bastieri, R. Bellazzini, B. Berenji, A. Berretta, E. Bissaldi, R. D. Blandford, et al. Incremental fermi large area telescope fourth source catalog. *The Astrophysical Journal Supplement Series*, 260(2):53, 2022.

[4] F. Aharonian, A. Akhperjanian, K.-M. Aye, A. Bazer-Bachi, M. Beilicke, W. Benbow, D. Berge, P. Berghaus, K. Bernlöhr, O. Bolz, et al. High-energy particle acceleration in the shell of a supernova remnant. *Nature*, 432(7013):75–77, 2004.

[5] F. Aharonian and A. Atoyan. Compton scattering of relativistic electrons in compact x-ray sources. *Astrophysics and Space Science*, 79:321–336, 1981.

[6] F. Aharonian, S. Kelner, and A. Y. Prosekin. Angular, spectral, and time distributions of highest energy protons and associated secondary gamma rays and neutrinos propagating through extragalactic magnetic and radiation fields. *Physical Review D—Particles, Fields, Gravitation, and Cosmology*, 82(4):043002, 2010.

[7] A. Atoyan and F. Aharonian. On the mechanisms of gamma radiation in the crab nebula. *Monthly Notices of the Royal Astronomical Society*, 278(2):525–541, 1996.

[8] W. Atwood, A. A. Abdo, M. Ackermann, W. Althouse, B. Anderson, M. Axelsson, L. Baldini, J. Ballet, D. Band, G. Barbiellini, et al. The large area telescope on the fermi gamma-ray space telescope mission. *The Astrophysical Journal*, 697(2):1071, 2009.

[9] O. De Jager and A. Harding. The expected high-energy to ultra-high-energy gamma-ray spectrum of the crab nebula. *Astrophysical Journal, Part 1 (ISSN 0004-637X), vol. 396, no. 1, Sept. 1, 1992, p. 161-172.*, 396:161–172, 1992.

[10] R. Dodson, D. Legge, J. Reynolds, and P. M. McCulloch. The vela pulsar's proper motion and parallax derived from vlbi observations. *The Astrophysical Journal*, 596(2):1137, 2003.

[11] D. Foreman-Mackey, D. W. Hogg, D. Lang, and J. Goodman. emcee: the mcmc hammer. *Publications of the Astronomical Society of the Pacific*, 125(925):306, 2013.

[12] P. Goldreich and W. H. Julian. Pulsar electrodynamics. *Astrophysical Journal, vol. 157, p. 869*, 157:869, 1969.

[13] G. Kanbach, Z. Arzoumanian, D. Bertsch, K. Brazier, J. Chiang, C. Fichtel, J. Fierro, R. Hartman, S. Hunter, D. Kniffen, et al. Egret observations of the vela pulsar, psr0833-45. *Astronomy and Astrophysics (ISSN 0004-6361), vol. 289, no. 3, p. 855-867*, 289:855–867, 1994.

[14] C. Kennel and F. Coroniti. Confinement of the crab pulsar's wind by its supernova remnant. *Astrophysical Journal, Part 1 (ISSN 0004-637X), vol. 283, Aug. 15, 1984, p. 694-709.*, 283:694–709, 1984.

[15] D. Khangulyan, F. A. Aharonian, and S. R. Kelner. Simple analytical approximations for treatment of inverse compton scattering of relativistic electrons in the blackbody radiation field. *The Astrophysical Journal*, 783(2):100, 2014.

[16] R. Manchester and S. Johnston. Polarization properties of two pulsars. *Astrophysical Journal, Part 2-Letters (ISSN 0004-637X), vol. 441, no. 2, p. L65-L68*, 441:L65–L68, 1995.

[17] R. N. Manchester, G. B. Hobbs, A. Teoh, and M. Hobbs. The australia telescope national facility pulsar catalogue. *The Astronomical Journal*, 129(4):1993, 2005.

[18] A. Pellizzoni, A. Trois, M. Tavani, M. Pilia, A. Giuliani, G. Pucella, P. Esposito, S. Sabatini, G. Piano, A. Argan, et al. Detection of gamma-ray emission from the vela pulsar wind nebula with agile. *Science*, 327(5966):663–665, 2010.

[19] S. Reynolds and R. Chevalier. Evolution of pulsar-driven supernova remnants. *Astrophysical Journal, Part 1 (ISSN 0004-637X), vol. 278, March 15, 1984, p. 630-648.*, 278:630–648, 1984.

[20] D. Thompson, C. Fichtel, D. Kniffen, and H. Ögelman. Sas-2 high energy gamma-ray observations of the vela pulsar. Technical report, 1975.

[21] M. Wood, R. Caputo, E. Charles, M. Di Mauro, J. Magill, and J. Perkins. Fermipy: An open-source python package for analysis of fermi-lat data. *arXiv preprint arXiv:1707.09551*, 2017.

[22] V. Zabalza. naima: a python package for inference of relativistic particle energy distributions from observed nonthermal spectra. *arXiv preprint arXiv:1509.03319*, 2015.